Results in Engineering 27 (2025) 106592

Contents lists available at ScienceDirect

Results in Engineering

journal homepage: www.sciencedirect.com/journal/results-in-engineering

Research paper

Experimental study on the seismic response of foundations: Impact of coral silt location on structural behavior during seismic events

Chunyong Jiang [a,b], Xuanming Ding [b,d], Qiang Ou [b,c,*], Jinqiao Zhao [b], Zhaogang Luo [b]

[a] Chongqing City Construction Investment (Group) Co., Ltd, Chongqing, 400015, China
[b] College of Civil Engineering, Chongqing University, Chongqing, 400045, China
[c] Department of Civil and Environmental Engineering, The Hong Kong Polytechnic University, Hung Hom, Kowloon, Hong Kong, 999077, China
[d] Hunan Provincial Key Laboratory of Intelligent Disaster Prevention–Mitigation and Ecological Restoration in Civil Engineering, Hunan Engineering University, Xiangtan 411104, China

ARTICLE INFO

Keywords:
Coral silt
Shaking table test
Liquefaction
Excess pore water pressure (EPWP)
Stress-strain

ABSTRACT

In coral reef hydraulic reclamation projects, particle sorting creates interbedded foundations composed of coral sand and silt within the reef structure. This study examined the seismic response of such foundations with varying positions of the coral silt layer using 1 g shaking table tests. The results showed that a coral sand foundation with the silt layer positioned in the middle exhibited greater overall stiffness during seismic activity compared to one with the silt at the bottom A middle located silt layer also alters the distribution of excess pore water pressure: the depth-distribution curve beneath the superstructure displayed a distinct turning point at the silt layer, with a significant increase in pressure within the silt and a reduction in the upper layers. At a peak ground acceleration (PGA) of 0.15 g, the middle silt layer substantially reduced both horizontal displacement and superstructure settlement, with settlement decreasing by 70.1 % compared to foundations with the silt at the bottom. In both configurations, shear strain decreases with depth, underscoring the influence of overburden pressure.

1. Introduction

Coral sand is a unique marine sediment derived from the skeletal remains of reef-building corals, calcareous algae, and other carbonate-producing organisms. Predominantly found in tropical and subtropical shallow marine environments, it forms through bioerosion and mechanical breakdown of coral reefs by waves, currents, and biological activity, producing fragmented particles ranging from coarse sand to silt-sized grains. Over time, these particles undergo further abrasion, chemical dissolution, and biogenic reworking, eventually accumulating as unconsolidated deposits on reef flats, lagoons, and adjacent coastal zones [30,31]. The grain size and composition of coral sand vary spatially, influenced by local hydrodynamic conditions, biological productivity, and geological history. For example, high-energy environments typically contain coarser, well-sorted sands, whereas sheltered areas tend to accumulate finer particles enriched with microfossils and organic matter [10,20,33].

A notable subset of coral sand is coral sand-silt, a mixed sediment formed through the prolonged weathering of coral fragments and the accumulation of silt-sized carbonate particles [34]. This transition from sand to silt results from physical reworking (e.g., wave action, bioturbation), chemical dissolution of aragonitic components, and microbial mediation, which accelerates particle breakdown. These processes produce a sediment with a distinct geotechnical profile marked by high compressibility and low shear strength, differentiating it from pure coral sand deposits [6,32].

In coral reef hydraulic reclamation projects, dredged coral sand and silt are hydraulically pumped to form artificial landmasses. During this process, particle sorting takes place as a result of differences in grain size, density, and settling velocity. This leads to the formation of heterogeneous, interbedded sand - silt foundations [37]. Under high - energy pumping conditions, coarser coral sand particles settle quickly, creating loose, permeable layers. In contrast, finer silt fractions (typically <0.075 mm) are transported over greater distances and deposited as low - permeability interlayers [21]. This stratification gives rise to alternating zones with contrasting hydraulic conductivity and shear

---

* Corresponding author.

E-mail addresses: chiangchunyung@163.com (C. Jiang), dxmhhu@163.com (X. Ding), ouq126@cqu.edu.cn (Q. Ou), zjqiao@cqu.edu.cn (J. Zhao), 20211601070@cqu.edu.cn (Z. Luo).

https://doi.org/10.1016/j.rineng.2025.106592
Received 7 July 2025; Received in revised form 22 July 2025; Accepted 2 August 2025

strength, which significantly impacts the mechanical behavior of the foundation [8,9].

Such interbedded systems are especially vulnerable to differential settlement, seepage erosion, and liquefaction when subjected to dynamic loads. For instance, silt layers function as obstructions to pore water dissipation. This exacerbates excess pore pressure during occurrences such as earthquakes or storm surges. Meanwhile, sand layers might experience rapid compaction [6]. Despite being common in reclaimed reef areas, the mechanical interactions between coral sand and coral silt beneath overlying infrastructure are still not well comprehended. The majority of studies concentrate on homogeneous coral sand or silt, overlooking the anisotropic characteristics of stratified systems [15]. This lack of knowledge presents risks to the long - term stability of island - engineering projects. This is demonstrated by post - construction failures in the South China Sea, where liquefaction - induced subsidence has caused damage to port facilities and runways [27].

Historical seismic events have time and again laid bare this susceptibility. In the 2010 South China Sea earthquake, the reclaimed coral sand foundations under a port facility underwent severe liquefaction. This led to a differential settlement of 40 centimeters and a 12-degree tilt of the container cranes, making the terminal non-functional for several months [27]. The 2015 earthquake in the Solomon Islands set off widespread liquefaction in coral sand embankments. Consequently, a 300-meter section of the runway collapsed, and the reconstruction costs amounted to $220 million [23]. Smaller seismic events, like the 2018 Philippine reef earthquake, brought about localized sand boils and foundation softening in residential buildings. This displacement affected more than 1,200 residents [2].

As an essential resource for island construction and coastal protection, the engineering behavior of coral sand, especially its tendency to liquefy under dynamic loading conditions, calls for thorough examination. The existing research has mainly centered on unit-scale studies of the liquefaction of coral sand and coral silt. Researchers have utilized cyclic triaxial tests and discrete element modeling to measure parameters such as liquefaction resistance and the evolution of pore pressure [6, 38]. Although these studies offer fundamental understandings of microscale processes, like particle crushing and the movement of fine particles, they inherently fail to account for the soil-structure interaction (SSI), which is crucial for the performance of infrastructure in real-world scenarios [18,35]. For example, unit-scale experiments are unable to simulate the intricate stress redistribution that is caused by overlying structures or the anisotropic impacts of the stratified sand-silt interbeds that are formed during hydraulic reclamation. These interbeds, which are formed due to particle sorting during the dredging process, give rise to alternating layers of highly permeable coral sand and low-permeability silt. These layers trap pore pressure and increase the risks of liquefaction [15,21].

The neglect of the soil-structure interaction (SSI) in present research methodologies results in substantial deficiencies in predicting hazards. Laboratory experiments conducted on homogeneous soil samples are unable to fully represent the combined effects of infrastructure loads, foundation geometry, and stratigraphic variability on failures triggered by liquefaction. This discrepancy is clearly observable in post-disaster evaluations. Borehole data obtained from the 2010 South China Sea seismic event showed that the silt interlayers contributed to an increase in pore pressure buildup. However, none of the previous models had taken these layered systems into consideration [21]. Likewise, centrifuge and shaking table tests, which have been established as effective means for studying SSI in terrestrial soils, have not been adequately employed in the study of coral sand. This is because of the difficulties encountered in replicating the crushable nature of its grains and its bio-cemented structure [16].

This study integrates sedimentological, geochemical, and geotechnical perspectives to fill this knowledge gap. Special attention is given to the role that the position of coral silt plays in governing soil - structure interactions. Through the implementation of advanced physical experiments, our goal is to offer insights that are crucial for the sustainable development of islands and the mitigation of hazards. The seismic response of coral sand foundations with different coral silt positions was examined using shaking table tests.

2. Experimental materials and test procedures

2.1. Test equipment and similarity ratio

The tests were conducted using a 1 g shaking table test system at Chongqing University. This system primarily consists of a power system, a control system, a shake table, and a laminar shear box, as illustrated in Fig. 1. The shake table measures 1.2 meters in both length and width, with a maximum allowable horizontal displacement of 100 mm. It can replicate both sinusoidal and real seismic waves, achieving a maximum amplitude of 2.0 g and operating within a frequency range of 0 to 50 Hz. A stainless-steel laminar shear box, with internal dimensions of 950 mm in length, 850 mm in width, and 700 mm in height, was employed to simulate the seismic response of the free field under one-dimensional shearing. Notably, the layers of the shear box are connected by roller bearings to minimize friction. To establish impervious boundary conditions, a white transparent plastic film, 12 threads thick, was inserted into the shear box.

Shaking table testing is an effective method for studying the dynamic response of foundations and structures under seismic loading. However, 1 g shaking table tests have limitations and often require certain simplifications [1]. In 1 g shaking table tests, the results can be used to qualitatively analyze soil liquefaction patterns, even though the stress levels differ from those encountered in the field [12,36,41,42]. In this experiment, the superstructure is involved, so the scaled-down model is designed according to Bockingham's π theorem. Based on the dimensions of the shaking table and its maximum acceleration capacity, a geometric similarity ratio of 1/40 was chosen for the superstructure. The similarity factors for the remaining geotechnical parameters are provided in Table 1. It is important to note that practical challenges arise when applying the similarity ratio to soil, particularly under soil liquefaction conditions [1]. Consequently, similarity ratios were not applied to the test material.

2.2. Test materials and superstructure

In this study, coral sand and coral silt were collected from a reef in the South China Sea. The grain size distribution curves for these test materials are shown in Fig. 2. The basic physical properties of the coral sand and coral silt are detailed in Table 2 and Table 3, respectively. Compared with the marine soils in other regions, the plastic limit of coral mud is relatively lower, which also leads to the differences in physical and mechanical properties between coral mud and the soils in other regions. These data came from Jiang et al. [19]. The maximum void ratio $e_{\max}$, minimum void ratio $e_{\min}$ and the specific gravity G_s of the coral sand were determined according to ASTM D4253 [4], ASTM D4254 [5], and ASTM D854 [3], respectively.

According to Ding et al. [11], the prototype superstructure in this study was a typical three-story reinforced concrete frame structure with a raft foundation. Such superstructures are commonly found on coral reefs in regions like the South China Sea, the Maldives, Guam, Hawaii, and Haiti. Due to the reduced size of the superstructure after scaling according to the geometric similarity ratio, constructing it with concrete was impractical. Consequently, the superstructure was made from organic glass, which has an elasticity modulus of 4.2 GPa, as depicted in Fig. 3. To achieve inertia force matching between the test model structure and the prototype structure, the incomplete counterweight method was employed in this study. The total weight of the model was 16.7 kg, achieved by attaching a 3.5 kg steel plate to each floor of the superstructure and a 6.2 kg steel plate to the bottom raft.

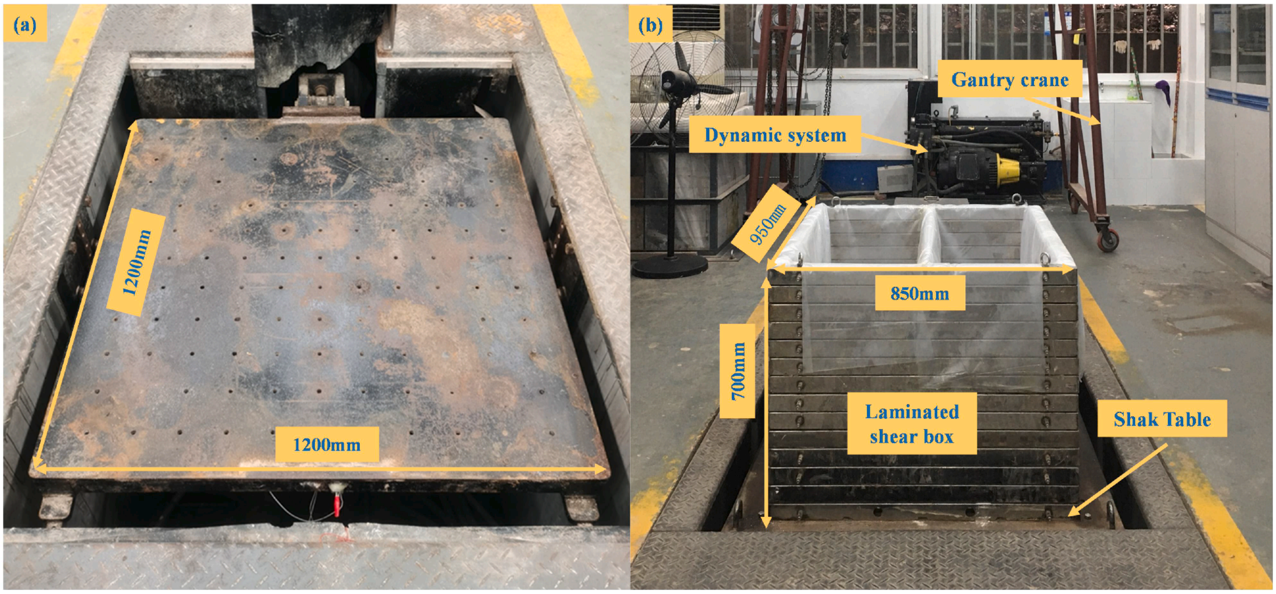

Fig. 1. Shaking table test systems.

Table 1
Similarity ratios of the model.

Parameter	Relationship	Similarity ratio
Length, *l*	S_l	1/40
Elastic modulus, *E*	S_E	3/20
Stress, *σ*	$S_\sigma = S_E$	3/20
Density, *ρ*	$S_\rho = S_E/(S_l S_a)$	6
Time, *t*	$S_t = S_l^{0.5} S_a^{-0.5}$	0.158
Frequency, *f*	$S_f = S_l^{-0.5} S_a^{0.5}$	6.325
Velocity, *v*	$S_v = S_l^{0.5} S_a^{0.5}$	0.158
Acceleration, *a*	$S_a = S_a$	1

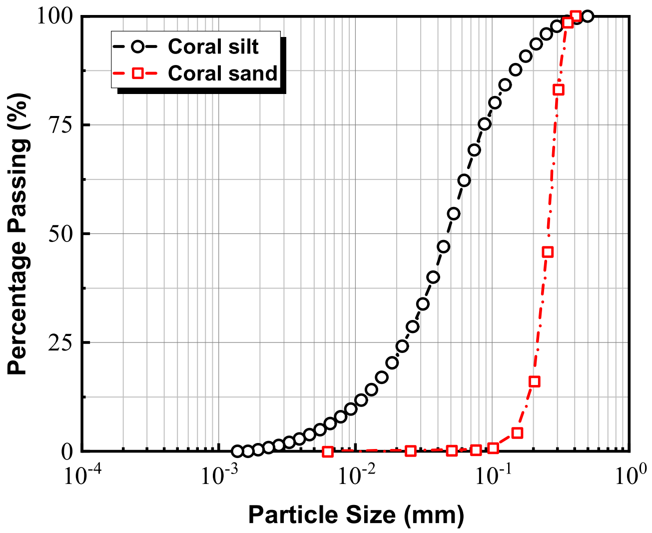

Fig. 2. Grain size distribution curves.

Table 2
Physical properties of coral sand.

Soil	G_s	e_{min}	e_{max}	C_c	C_u
Coral sand	2.78	0.82	1.09	1.6	10

Table 3
Physical properties of coral silt.

Soil	G_s	Plastic limit/%	Liquid limit/%	Plasticity index/I_p
Coral silt	2.77	21.73	32.98	11.24

2.3. Model setup and instrumentation

To ensure uniformity in the model foundation, the water sedimentation method was used during its construction, as described by Li et al., [26]. Research has shown that the fall distance is a key factor affecting the relative density of the prepared model foundation. Therefore, it was essential to calibrate the drop height before model preparation. A drop height of 10 cm was used to achieve a relative density of 65 % for the coral sand. This study investigated the seismic response characteristics of coral sand foundations with varying silt positions under seismic loading.

The shear box was evenly divided into two sections with dividers aligned in the direction of vibration. In one section, a layer of coral silt covered the foundation bottom, with coral sand layered above it. The other section featured a layer of coral silt positioned in the middle of the coral sand foundation. Model preparation involved several steps: scales were marked along the height of the shear box to assist in layering the samples and placing sensors. The model foundation was then constructed in six layers, each corresponding to 10 cm. For the coral sand layer, the specified amount of coral sand for each layer was poured into a hopper, which evenly distributed the sand into the shear box. During the construction of the coral sand layer, a 10 cm free water level was maintained to ensure full saturation, as recommended by Li et al., [26] and Orang et al., [29]. Meanwhile, the drop height was consistently controlled to achieve the target relative densities. For the coral silt layer, the appropriate amount of silt for each layer was mixed with water and carefully placed into the shear box. The superstructure was positioned at the center of the top of the soil model. Finally, a 30 mm thick layer of dry sand was added on top of the model using the dry pluviation method, as described by Orang et al., [29], to simulate real engineering conditions. The final height of the model foundation was approximately 63 cm. Before applying dynamic loads, the model was left undisturbed for 24 hours, following the guidelines of Ding et al., [11] and Ding et al., [12].

To investigate the seismic responses of the superstructure and foundation, various sensors were installed to measure pore water

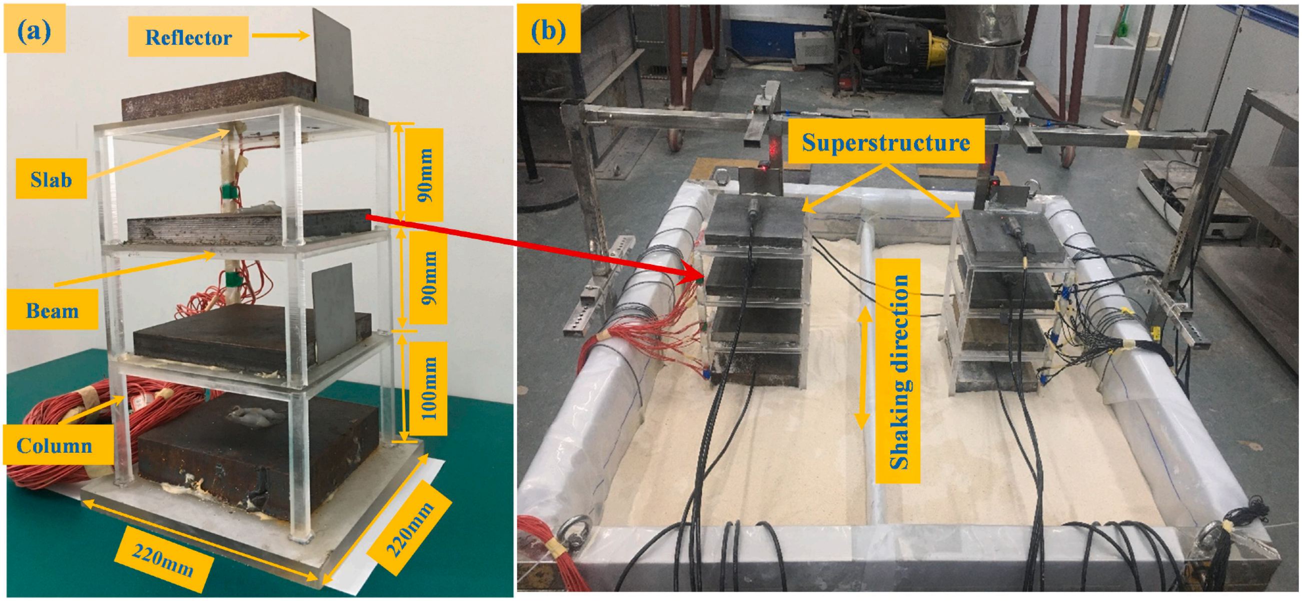

Fig. 3. Illustration of the test model: (a) superstructure and (b) test model.

pressure, accelerations, horizontal and vertical displacements, and strain at different locations within the model. Fig. 4 illustrates the model soil profile and the instrumentation plan for these two shaking table tests.

An array of accelerometers was strategically placed at the center to capture the acceleration responses of both the superstructure and the foundation. Two arrays of pore water pressure sensors were used to measure pore pressure at various depths within the foundation, with one array positioned at the center and the other 200 mm away. Additionally, a row of pore pressure sensors was deployed to capture pore pressure at different horizontal positions from the center. Three laser displacement sensors measured the settlement and horizontal displacement of the superstructure. Strain gauges were installed at various heights of the superstructure to measure strain, with detailed information provided in Fig. 4(b) and 4(c).

2.4. Sequences of shaking

In this study, two shaking table tests were conducted to investigate the seismic response of coral sand foundations with varying placements of coral silt, as detailed in Table 4. The relative density was set 65 % which represents a moderate compactness state. In this experiment, it is sufficient to maintain the compactness of the soil layer during the test and keep it basically the same as the actual compactness. These tests aimed to understand how different silt locations affect the foundation's behavior during seismic events. A sine wave was used as the seismic input due to its simpler pattern compared to natural seismic waves, making it more convenient for analyzing the seismic response. The input sine wave excitation is illustrated in Fig. 5. The two shaking sequences differed only in their peak accelerations, while maintaining the same duration and frequency. To assess the system's baseline response and any changes due to the sinusoidal input, white noise with an amplitude of 0.02 g was applied to the model for 20 seconds both before and after each sinusoidal excitation. Acceleration amplitude of 0.1 g represents intensity of a magnitude 7 earthquake.

3. Results and discussion

3.1. Macroscopic phenomena

The macroscopic phenomena of the model before and after the shaking table model test were depicted in Fig. 6. Prior to applying the input motion, the foundation surface was leveled, and the superstructure was horizontally calibrated, as shown in Fig. 6(a). At a peak ground acceleration (PGA) of 0.1 g, the ground surface of the models in both Case-1 and Case-2 remained largely unchanged, with no water seepage observed. A slight swaying of the superstructure was noted, but there was no significant subsidence. When the input motion increased to 0.15 g, the superstructures in Cases-1 experienced violent shaking due to the vibration excitation, and large cracks appeared along the perimeter of the raft foundation.

As the vibration continued to 2 seconds in Case-1, the ground surface of the foundation began to bulge, indicating significant liquefaction. This was evidenced by the subsidence of the superstructure, which was followed by a gradual tipping. During the process, seepage occurred on the ground surface in Case-1, leading to a rapid accumulation of water. In contrast, the ground surface around the foundation perimeter in Case-2 did not begin to bulge until 7 seconds into the input motion, with only slight settling of the superstructure. Simultaneously, water started to seep around the perimeter and accumulated on the ground surface by the end of the vibration. At the conclusion of the vibration, the superstructure was tilted by 17 degrees in Case-1 and 0.5 degrees in Case-2. A comparison between Case-1 and Case-2 revealed that Case-1, which had coral silt at the bottom with better drainage channels, allowed water to seep to the ground surface more quickly than Case-2. It was evident that after the test, the superstructure in Case-1 experienced severe tilting and subsidence. In contrast, the superstructure in Case-2 exhibited only slight subsidence.

The shaking table test in this paper was conducted under a 1 g condition. There is a certain difference in the stress level of the foundation compared to the actual condition. Those tests are conducted under 1 g, which restricts the ability to accurately replicate the in-situ stress conditions present in the field, particularly the confining pressures experienced at depth. scaling effects present a challenge; while geometric scaling can be achieved, it is not possible to simultaneously satisfy all similitude requirements for stress, strain, and time under 1 g conditions. The test results can be used to qualitatively analyze the influence of coral mud interlayers on the dynamic response of the foundation under seismic load. In future research, centrifuge shaking table tests can be carried out using centrifuge equipment.

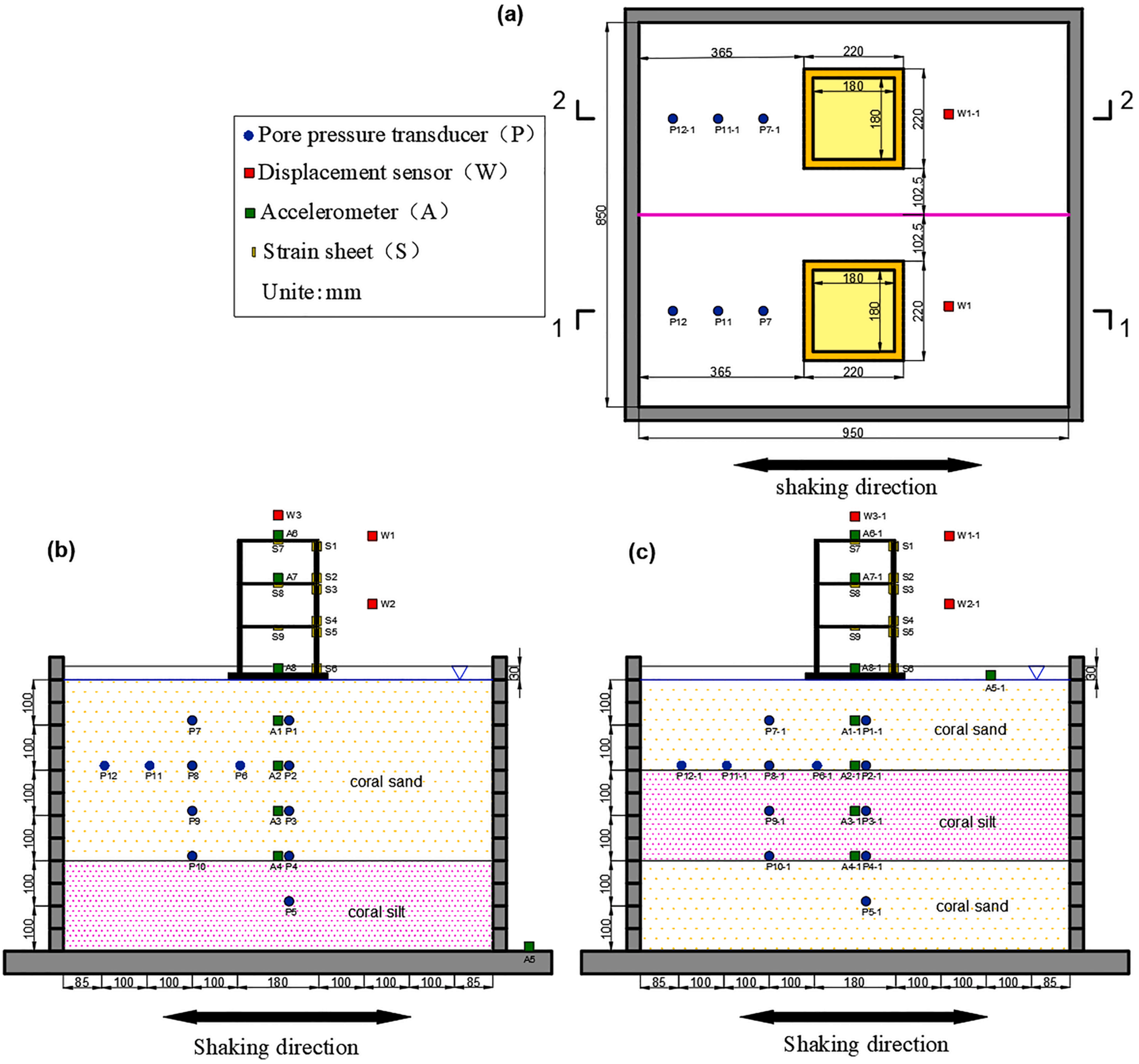

Fig. 4. Model soil profile and instrumentation plan: (a) plan layout diagram; (b) elevation view along section 1-1 and (c) elevation view along section 2-2.

Table 4
Shaking table test cases.

No.	Coral Silt Position	Relative density	Acceleration amplitude (g)	Input motion
Case-1	coral silt covering the bottom	65 %	0.1, 0.15	Sin_5 Hz
Case-2	coral silt situated in the middle	65 %	0.1, 0.15	Sin_5 Hz

3.2. *Acceleration response*

When the peak ground acceleration (PGA) was 0.1 g, the acceleration time history curves for both Case-1 and Case-2 exhibited no significant attenuation, with similar development patterns observed across all positions. For instance, Fig. 7(a) displays the curves at position A1 in the foundation and position A6 at the top of the superstructure. At a PGA of 0.15 g, the acceleration time history curves for Case-1 and Case-2, as shown in Fig. 7(b), can be roughly divided into three distinct stages. In Stage 1 (approximately 0 to 1 second), the acceleration response in both the foundation and superstructure peaked because of the vibration excitation. The similarity in acceleration responses between Case-1 and Case-2 at all positions suggests that liquefaction did not occur during this stage, and the foundation soil retained a high shear transfer capacity.

In Stage 2 (approximately 1 to 9 seconds), despite the constant input motion, the acceleration response in both the foundation soil and superstructure began to attenuate. Notable differences in attenuation patterns were observed between the cases and positions. In Case-1, positions A1, A2, A3, A4, and A8 exhibited similar attenuation patterns, with the acceleration response decreasing after peaking and reaching a minimum around 3 seconds, then stabilizing as the vibration continued. However, position A6 showed a slightly different pattern, with a larger peak occurring later than at other positions.

In contrast, Case-2 displayed some variations in attenuation patterns. Positions A1 and A2 followed a similar trend to Case-1, though the

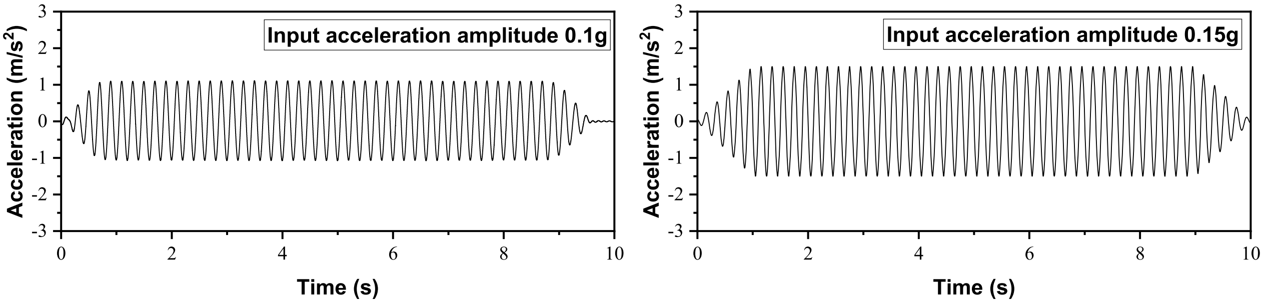

Fig. 5. Input sine wave excitation.

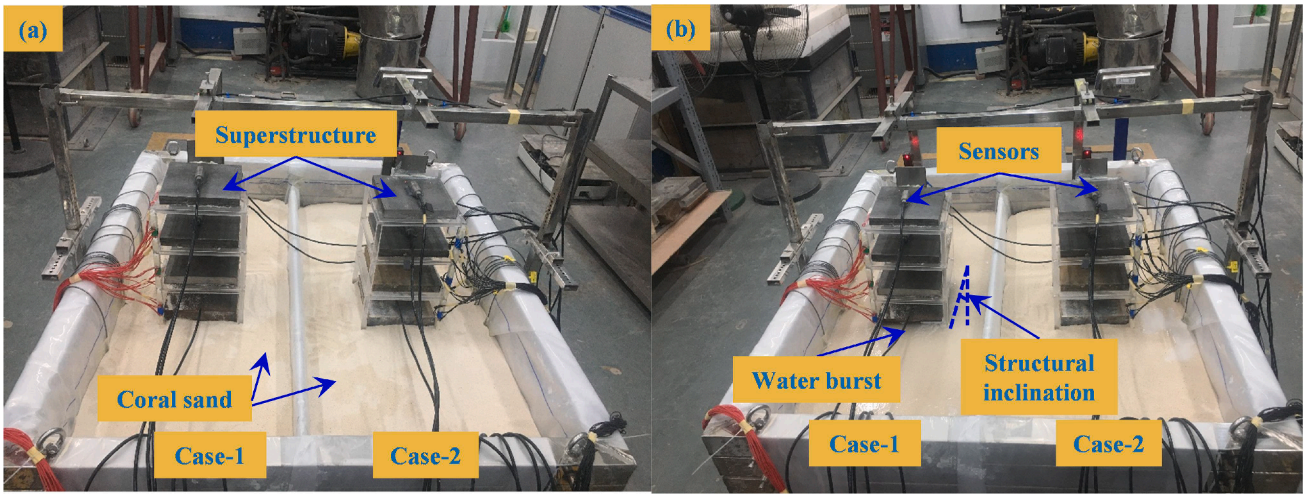

Fig. 6. Macroscopic phenomena of model (a) before texting; (b) after testing.

acceleration amplitude was higher in Case-2. Positions A3 and A4 in Case-2 differed, with the acceleration response decreasing after peaking and hitting a minimum around 1-2 seconds, then gradually increasing again until the end of the stage. This difference may be attributed to the material composition, as positions A1 and A2 were in coral sand, while positions A3 and A4 were in coral silt. Additionally, the acceleration at positions A1, A2, A6, and A8 reached their peak values and then decreased to a stable level with the input motion until the stage concluded.

In Stage 3 (approximately 9 to 10 seconds), the input excitation decreased from its peak value to zero, and the corresponding acceleration response also diminished to zero. Overall, the foundation in Case-1 exhibited greater acceleration attenuation compared to Case-2, suggesting a higher degree of liquefaction in Case-1, particularly in the upper region of the foundation.

By comparing the peak acceleration amplification coefficients from positions A1 to A8 in Case-1 and Case-2 under different seismic loads, the variation of these factors along the depth was analyzed. Fig. 8 illustrates the peak acceleration amplification factors for both cases at PGAs =0.1 g and 0.15 g. It is evident that the amplification factors gradually increase from the bottom to the top in both Case-1 and Case-2, regardless of the seismic excitation amplitude, indicating an amplification effect along the depth. Additionally, the amplification effect is more pronounced above the soil surface compared to below it. Comparing Case-1 and Case-2, it was evident that the peak acceleration amplification factor in Case-2 was larger than in Case-1 at heights between 40 cm and 60 cm. Conversely, for other heights, the amplification factor in Case-2 was smaller than in Case-1. The 40 cm to 60 cm layer consists of coral silt, suggesting that coral silt can increase the peak acceleration amplification factor of the soil. For instance, at position A1, the peak acceleration amplification factors for Case-1 and Case-2 were 1.45 and 1.49 at a PGA of 0.1 g, and 1.62 and 1.65 at a PGA of 0.15 g, respectively. This indicates that the overall stiffness of the coral sand-silt layer in the middle is greater than that of the coral silt layer at the bottom when subjected to seismic action.

3.3. *Excess pore water pressure*

Fig. 9 presented the time history curves of the excess pore water pressure (EPWP) ratio, r_u, which is defined as the ratio of EPWP to the initial effective overburden stress, at various depths. These observations were made in a coral sand foundation, characterized by a coral silt layer at the bottom and another situated in the middle. The soil is deemed preliminarily liquefied when r_u reaches 0.8, indicating the onset of cyclic fluidity and significant strain development [12,13,25,28].

Under seismic loading with a peak ground acceleration (PGA) of 0.1 g, the time history curves of r_u in Case-1 exhibited a consistent pattern across all positions (P1, P2, P3, P4, P5). Initially, the values increased rapidly and then stabilized as the seismic excitation rose from zero to its peak and remained there for a significant duration. As the seismic excitation decreased from its peak back to zero, the excess pore water pressure (EPWP) began to dissipate slowly, though it retained a residual level for a short period. In Case-1, the r_u values at all positions remained below 0.8, indicating no liquefaction occurred in the foundation.

In contrast, while the r_u values at positions P1, P2, and P3 in Case-2 were below 0.8, positions P4 and P5 exceeded this threshold, indicating liquefaction due to the presence of a coral silt layer in the middle of the coral sand foundation. Comparing the r_u curves for P1 to P3 reveals that EPWP in Case-1 dissipated more rapidly at the end of the seismic excitation than in Case-2. Conversely, the r_u curves for P4 and P5 showed slower dissipation in Case-1 compared to Case-2. This difference was attributed to the foundation composition: Case-1 had coral silt at the

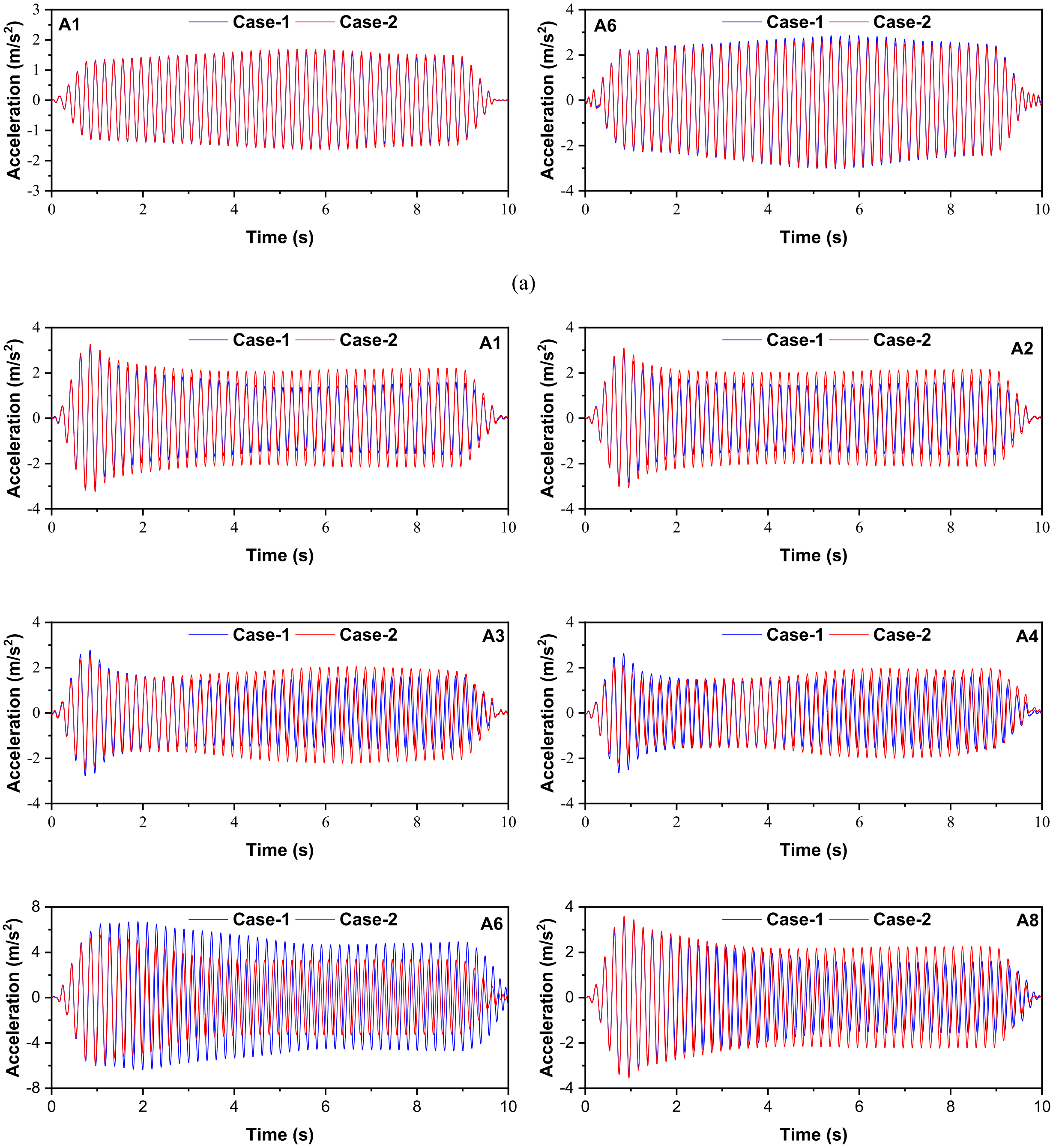

(a)

(b)

Fig. 7. Acceleration time history curves for case-1 and case-2 at PGA of (a) 0.1 g and (b) 0.15 g.

bottom, allowing drainage channels above the coral silt to remain unaffected, whereas Case-2′s coral silt layer in the middle acted as a barrier due to its lower permeability, hindering drainage and affecting EPWP dissipation rates.

The time history curves at positions P7 to P10 in Case-1 also followed a similar pattern, indicating EPWP dissipation. At positions P7 and P8, EPWP in Case-2 was smaller than in Case-1, while at other positions, it was greater, highlighting the inhibitory effect of coral silt on pore water pressure dissipation. Liquefaction was observed at P10 within the coral silt layer. The r_u curves at positions P2, P6, P8, P11, and P12 showed similar patterns for both Case-1 and Case-2, with EPWP in Case-1 being greater than in Case-2.

When the input acceleration amplitude increased to 0.15 g, a notable difference emerged in the development pattern of excess pore pressure between Case-1 and Case-2, compared to the pattern observed at an amplitude of 0.1 g, as illustrated in Fig. 9(b). The excess pore pressure ratio quickly reached a peak and remained relatively stable after the seismic load was applied, then gradually decreased as the input excitation diminished from its peak value to zero. In Case-2, positions P1, P2, P6, P7, P8, P11, and P12, which are located above the coral silt layer, exhibited different variation patterns of pore water pressure compared to those beneath the coral silt. This difference can be attributed to the obstructive effect of the coral silt layer on pore water pressure dissipation. The coral silt acts as a barrier, affecting the drainage and pressure

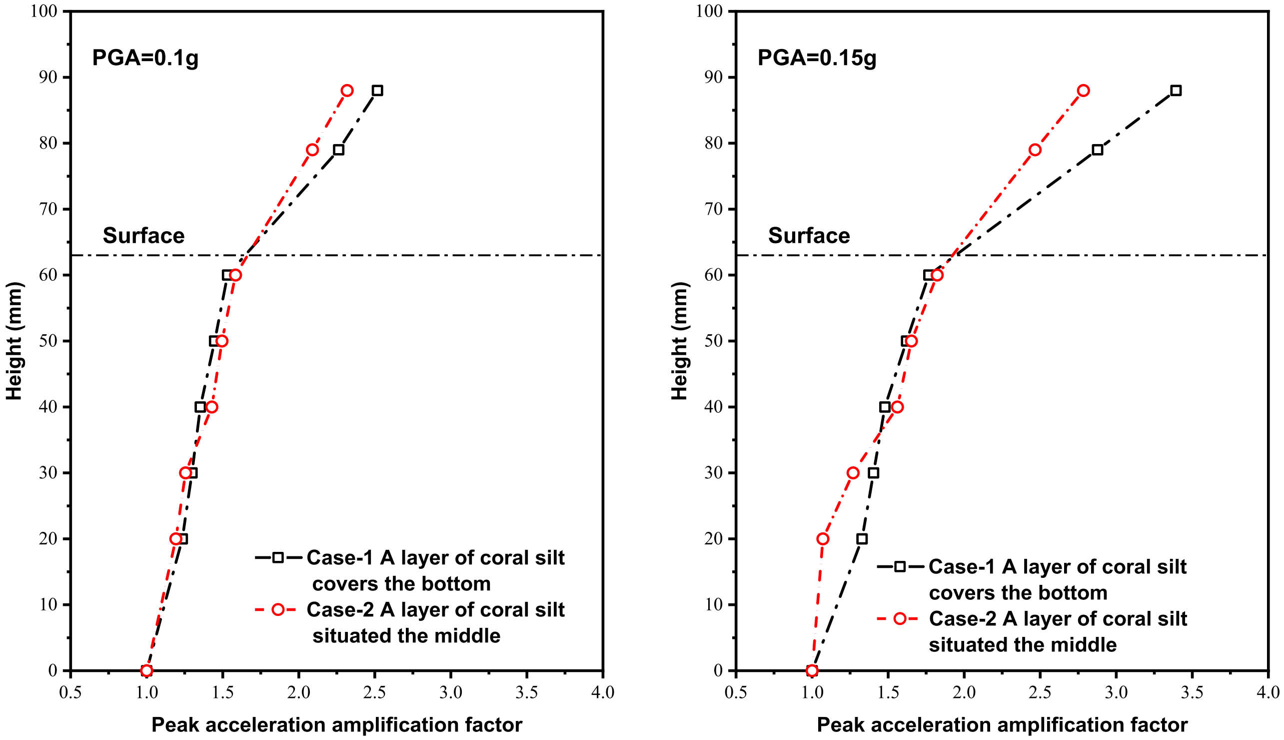

Fig. 8. Peak acceleration amplification coefficient.

dissipation at these points, leading to distinct behavior in the excess pore pressure development.

Fig. 10 illustrated the distributions of the excess pore water pressure ratio (r_u) along the depth in the region directly beneath the superstructure for both Case-1 and Case-2 at PGAs of 0.1 g and 0.15 g.

At a PGA of 0.1 g in Case-1, the r_u distributions remain largely unchanged or slightly decrease between heights of 20 cm to 50 cm. The development of excess pore water pressure (EPWP) in the upper region was inhibited by the structural loads, resulting in no significant increase in r_u at positions P1, P2, P3, and P4 in the middle region. However, at a height of 10 cm, r_u significantly increases due to the presence of the coral silt layer, which impedes drainage.

When the PGA increases to 0.15 g, the r_u distributions in Case-1 showed an upward trend with increasing height. In Case-2, the r_u curves at both PGAs of 0.1 g and 0.15 g followed a similar pattern: r_u initially increases with height, then decreases rapidly, and the decreasing trend gradually weakens, forming an approximate oblique "Z" shape. At a height of 10 cm and 20 cm, r_u exceeded 1.0 due to the coral silt layer's low permeability, which acted as a barrier to water movement.

Under seismic excitation, EPWP was generated in the foundation, and because the upward dissipation channel was blocked, r_u at P5 reaches a high value of 1.18. In the middle region of the foundation, r_u changed from 0.50 to 1.67 at positions P2 to P4 as excess pore water moved upward. At P1 in the upper region, the absence of recharge from the lower region and proximity to the ground surface, along with a smooth drainage channel, result in a relatively low r_u of 0.29. The values at P4 and P5 exceed 0.8, indicating a liquefied state.

Fig. 11 illustrated the distribution of the excess pore pressure ratio (r_u) to the left of the superstructure for both Case-1 and Case-2. In both cases, r_u varied similarly with depth at PGAs of 0.1 g and 0.15 g. In Case-1, the excess pore pressure ratio increased with height, and as the PGA amplitude rase from 0.1 g to 0.15 g, r_u at all points exceeded 0.8, indicating a liquefied state throughout the foundation. In Case-2, although r_u also increased at all points, an inhibitory effect was observed at heights of 30 cm and 40 cm. This suggested that certain factors, possibly related to the composition or structure of the foundation, were limiting the increase in pore pressure at these specific depths.

Fig. 12 illustrated the distribution pattern of the excess pore pressure ratio (r_u) along the horizontal direction at a height of 40 cm from the bottom for both Case-1 and Case-2. In Case-1, r_u values increased with distance from the center at PGAs of 0.1 g and 0.15 g. This occurred because the development of excess pore water pressure (EPWP) was constrained directly beneath the superstructure during vibration, whereas EPWP can develop more freely at locations further from the center. Consequently, regions farther from the center exhibit more fully developed EPWP and higher r_u values. For example, at a PGA of 0.15 g, r_u at P2 (directly below the superstructure) is 0.73, while at P12 (40 cm away from the center), it is 1.29, marking an increase of approximately 74 %. In Case-2, the horizontal distribution pattern of r_u was generally like Case-1, with values increasing with distance from the center at both PGA levels, except at P8. The decrease in r_u at P8 was due to a through crack in the coral silt layer during vibration, which facilitated upward dissipation of EPWP, reducing pressure at this point. Overall, r_u values were larger in Case-1 than in Case-2 at both PGA levels, indicating the coral silt layer in Case-2 had a pronounced water barrier effect, impeding EPWP development and dissipation, resulting in lower r_u values compared to Case-1.

3.4. Horizontal displacement and settlement response

The time histories of superstructure horizontal displacement for Case-1 and Case-2 at PGA levels of 0.1 g and 0.15 g were illustrated in Fig. 13. Based on previous analysis, no liquefaction occurred in the foundation at PGA=0.1 g, indicating that the soil maintained a high shear transfer capability. Consequently, the horizontal displacements of the superstructure under PGA=0.1 g for both cases were minimal and nearly symmetric, as depicted in Fig. 13(a). For instance, at location W1, the maximum horizontal displacements for Case-1 and Case-2 were 1.95 mm and 1.82 mm, respectively, further confirming the absence of significant liquefaction in the foundations.

The horizontal displacements for Case-1 and Case-2 at PGA=0.15 g

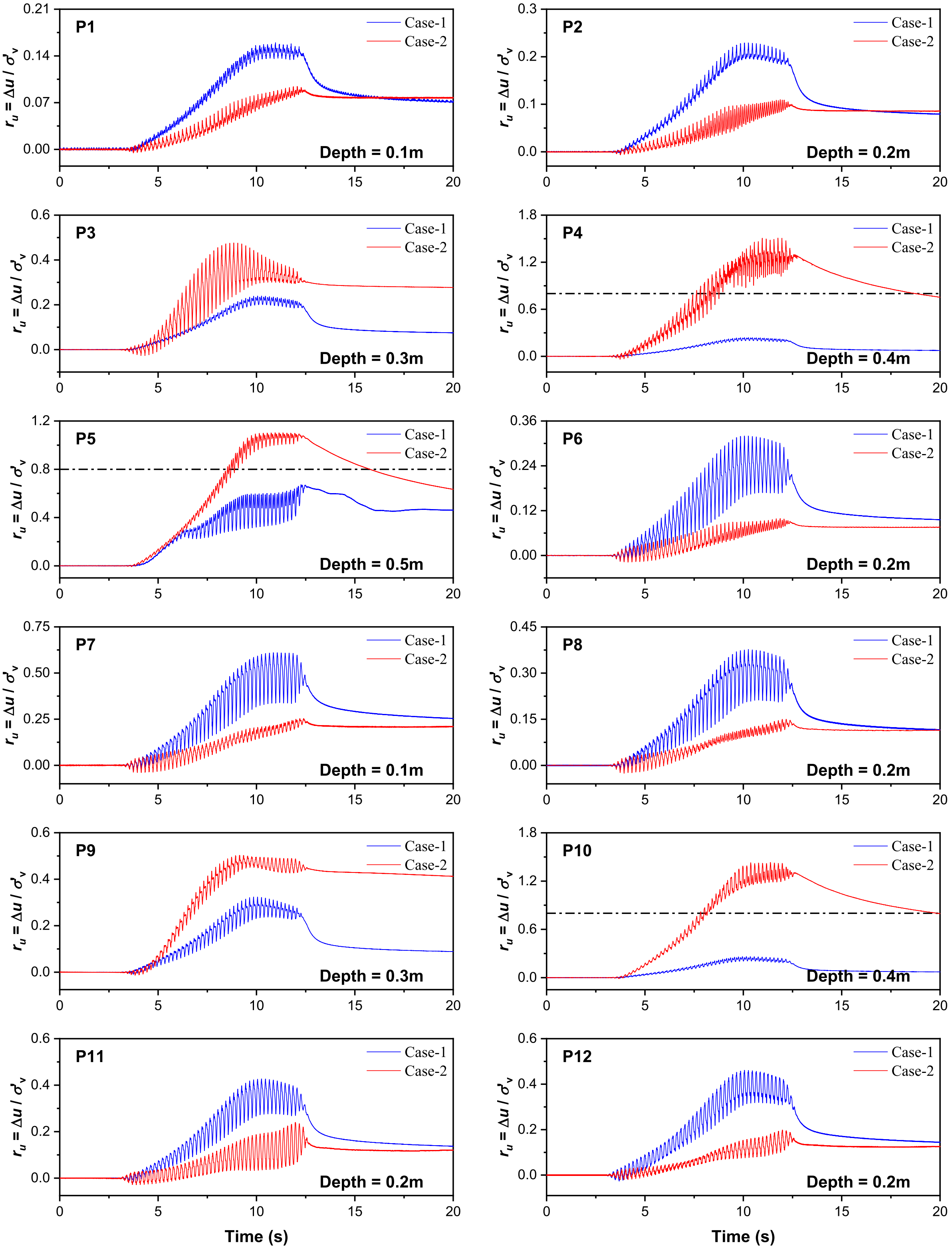

(a)

Fig. 9. Time history curves of excess pore water pressure ratio for Case-1 and Case-2 at PGA of (a) 0.1 g and (b) 0.15 g.

were shown in Fig. 13(b). In Case-2, the horizontal displacement of the superstructure at W1 and W2 peaked approximately 0.75 seconds after the seismic excitation began, then gradually decreased over the next 3 seconds, remaining stable until about 10 seconds, and finally decreased to zero by the end of the test. The time history curve of horizontal displacement was nearly symmetric from the onset of seismic excitation

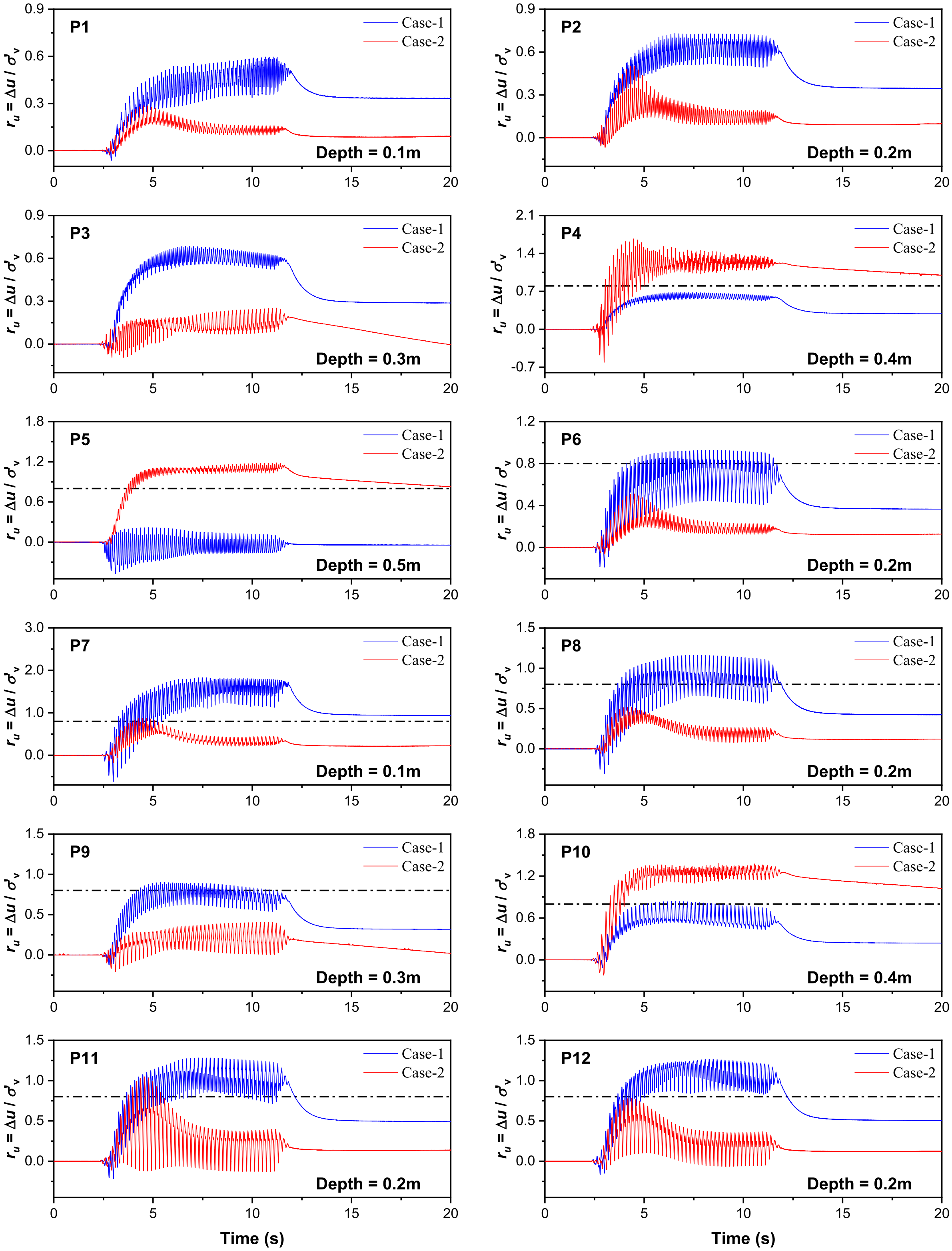

(b)

Fig. 9. (*continued*).

to the end, exhibiting no significant cumulative displacement, only cyclic displacement. Specifically, the maximum cyclic displacement at W1 was 6.4 mm. This suggests that the soil in the upper region of the foundation in Case-2 retained sufficient effective stress and shear strength to support the superstructure, resulting in almost no noticeable tilt after the vibration.

In contrast, in Case-1, the laser displacement sensor failed around 10 seconds. Cumulative horizontal displacement began to develop after the cyclic displacement reached its peak, with a relatively stable phase of cumulative displacement occurring before sensor failure. At this point, the cumulative horizontal displacements at W1 and W2 were 15.61 mm and 12.73 mm, respectively. Observations during the test confirmed that the superstructure experienced significant settlement and noticeable tilt following the liquefaction of the foundation.

The time history curves of superstructure settlement for Case-1 and Case-2 at PGA levels of 0.1 g and 0.15 g are presented in Fig. 14. As illustrated in Fig. 14(a), both cases exhibited a similar trend where settlement gradually increased with the onset of vibration and stabilized by the end of the test. However, the increase in settlement was more pronounced in Case-2. At the final stage, the superstructure settlement was 1.32 mm for Case-1 and 3.007 mm for Case-2.

At a PGA of 0.15 g, as shown in Fig. 14 (b), the settlement of the superstructure in Case-2 increased rapidly at the beginning and then continued to rise at a slower rate until the end of the vibration, resulting in a final settlement of 4.978 mm. In contrast, in Case-1, the settlement initially increased gradually and then stabilized until the test concluded. The final settlement for Case-1 was 16.64 mm, which is approximately 3.3 times greater than that of Case-2.

Building on the previous analysis, the variation pattern observed in Case-1 can be attributed to the gradual sinking of the superstructure following the liquefaction of the foundation. Initially, the area directly beneath the superstructure was not fully liquefied and retains some effective stress, resulting in relatively small overall settlement for both Case-1 and Case-2. At a PGA of 0.1 g, which corresponds to low seismic intensity, the deformation resistance of coral sand was greater than that of coral silt. Consequently, the final settlement in Case-2 was greater than in Case-1.

As the vibration continues, the degree of liquefaction increases, leading to a gradual increase in superstructure settlement due to the reduction in effective stress. At a PGA of 0.15 g, liquefaction occurred in Case-1, causing the soil at certain points to enter a fluid state, with effective stress nearly reduced to zero. This resulted in a sharp sinking of the superstructure, consistent with test observations. In contrast, liquefaction had not yet occurred in Case-2. In Case-2, the coral silt in the middle acts as a barrier to pore water pressure drainage and serves as a vibration isolation layer. Therefore, the settlement in Case-2 did not continue to increase and remained significantly smaller than in Case-1. In actual engineering projects, it is possible to appropriately add coral silt in sandy soil layers to reduce the liquefaction of the upper layers and the settlement deformation caused by earthquakes.

From the previous analysis of the EPWP ratio response, as shown in Fig. 10, the coral sand directly beneath the superstructure did not reach liquefaction (r_u=0.28) at PGA=0.15 g and retained a substantial amount of effective stress. This explains why the settlement of the superstructure in Case-2 was smaller than in Case-1.

Comparing Fig. 14, the settlement in Case-1 increased from 1.32 mm to 16.636 mm, while the settlement in Case-2 increased from 3.007 mm to 4.978 mm as the PGA increased from 0.1 g to 0.15 g. This further indicates that the foundation in Case-1 experienced liquefaction, whereas the changes in settlement for Case-2 were not significant. The coral silt layer within the coral sand effectively prevents the dissipation of pore water pressure and mitigates vibration effects.

3.5. *Superstructure bending moment*

When the peak ground acceleration (PGA) reached 0.1 g, the bending moment time history curves for both Case-1 and Case-2 exhibited minimal attenuation, with nearly identical development patterns across different positions. Fig. 15 illustrated the variation of the bending moment time history curves at position S1 (top of the superstructure) and S6 (bottom). At a PGA of 0.15 g, the bending moment time history curves for Case-1 and Case-2 were presented in Fig. 16. These curves can be broadly categorized into three distinct stages. In stage 1, the bending moment response in the superstructure peaked immediately upon vibration excitation. Notably, Case-1 and Case-2 displayed clear differences in bending moment response at each position. In Case-1, the time to reach peak bending moment was longer than in Case-2, and the peak value itself was also higher. In stage 2, Despite the constant input motion, the bending moment response in the superstructure began to attenuate. The attenuation patterns differed between the two cases and

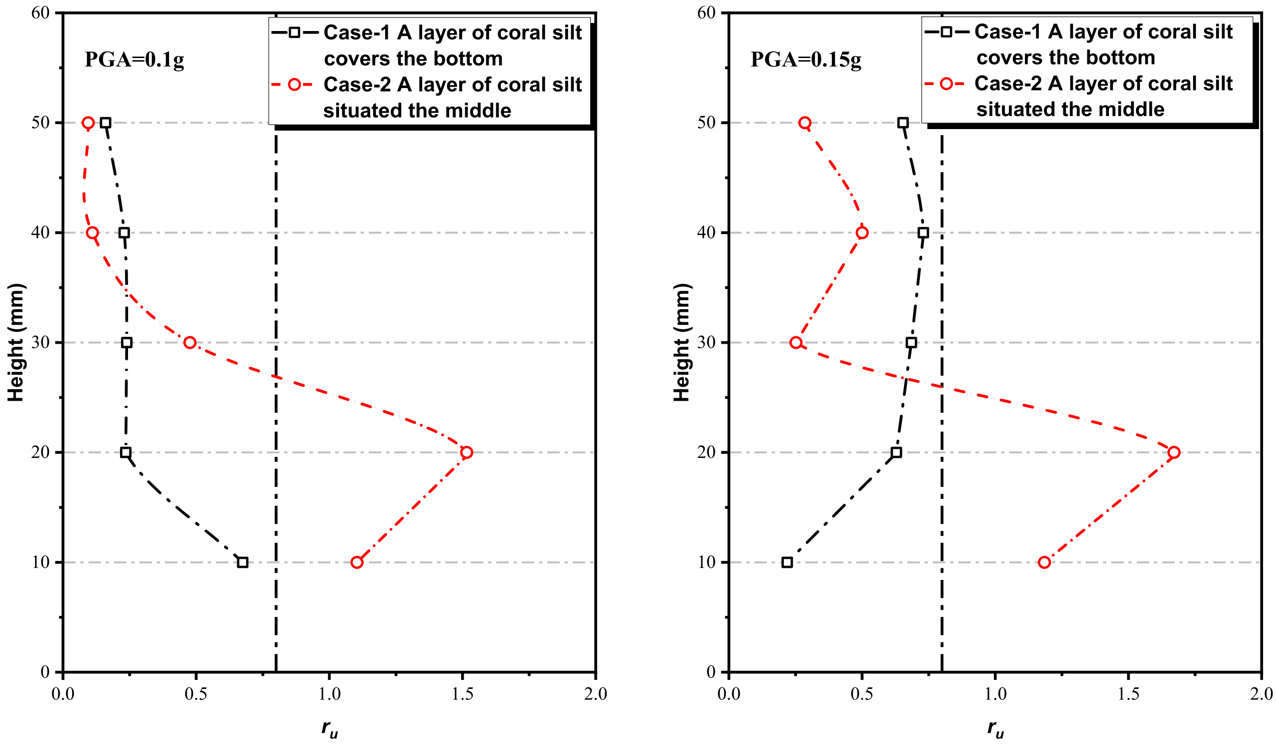

Fig. 10. Distribution curves of excess pore pressure ratio directly below the superstructure for Case-1 and Case-2.

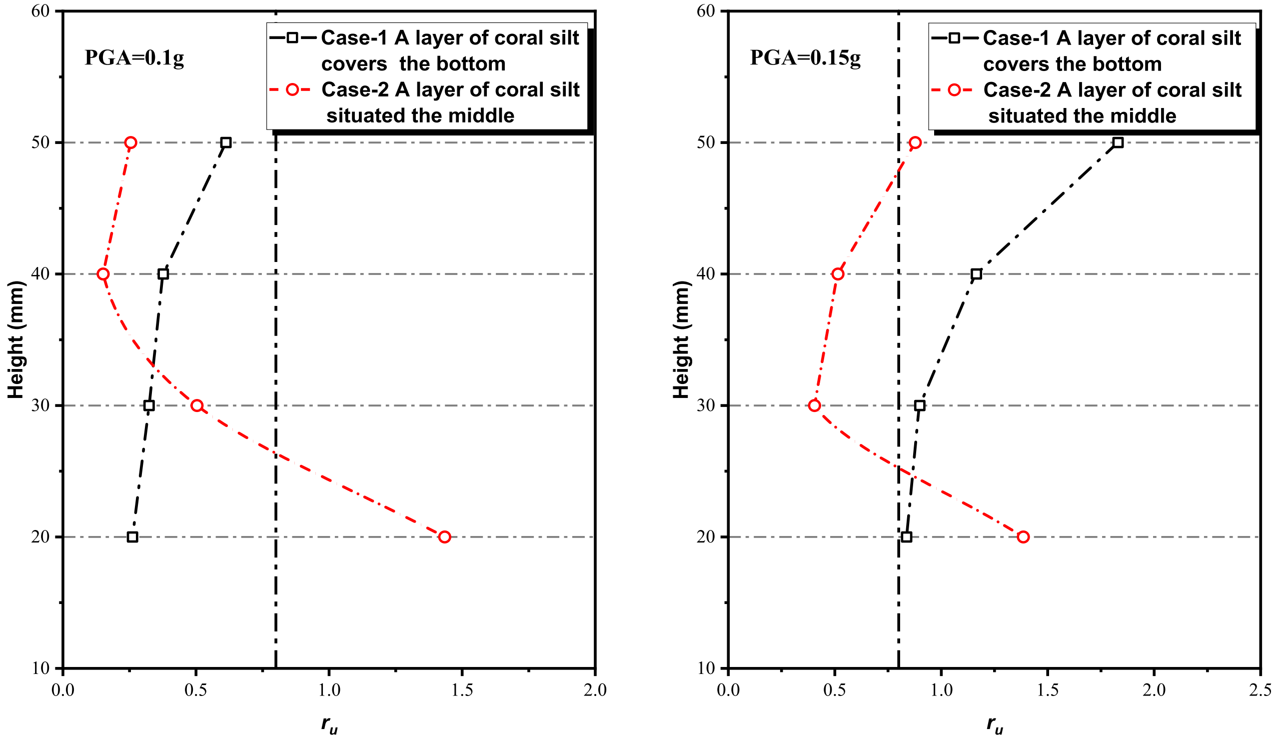

Fig. 11. Distribution curves of excess pore pressure ratio to the of the superstructure for Case-1 and Case-2.

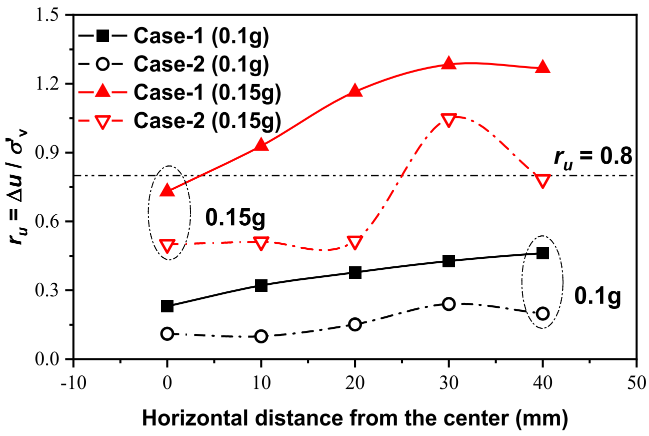

Fig. 12. Horizontal distribution curves of excess pore pressure ratio for Case-1 and Case-2.

across positions. For Case-1, the attenuation patterns at various positions were similar. After peaking, the bending moment response decreased, reaching a minimum value at approximately 3 seconds, then gradually increased again until the end of the stage. In contrast, Case-2 exhibited some differences in the attenuation patterns. After reaching its peak, the bending moment response dropped to a minimum in less than 3 seconds, then remained stable until the stage concluded. In stage 3, the input excitation decreased from its peak to zero, and the corresponding bending moment response also diminished to zero. Overall, the superstructure in Case-1 experienced a greater bending moment response than that in Case-2. This suggests that Case-1 was subjected to greater loads, indicating a lower bearing capacity of the foundation and a higher degree of liquefaction compared to Case-2.

3.6. Stress-strain behavior across various depths

The stress-strain relationship is essential for analyzing the shear modulus and damping ratio of soils under dynamic loading. However, directly measurement of stress and strain of soil during shaking table test can be challenging. Previous studies have demonstrated that these parameters can be derived from acceleration data, enabling researchers to infer soil behavior under seismic loading [24,39]. This approach uses recorded accelerations to estimate the shear forces and deformations, offering valuable insights into soil mechanical under dynamic conditions. The calculated shear stress represents the stress at the center of each soil element, which is the midpoint between acceleration measurement points. It is determined by summing the horizontal inertial forces of the overlying soil. This method has been widely adopted in studies the foundations seismic response [7,14,17,22]. Assuming shear wave propagation follows a one-dimensional shear beam model, shear stress and shear strain can be estimated using measured accelerations. By applying linear interpolation between acceleration data points, the shear stress and shear strain at any depth z_i can be expressed as follows [24,39]:

$$\tau(z_i,t)=\sum_{k=1}^{i-1}\rho\frac{a(z_i,t)+a(z_{i+1},t)}{2}\Delta z_i, i=2,3\cdots \tag{1}$$

$$\gamma(z_i,t)=\frac{1}{\Delta z_{i-1}+\Delta z_i}\left[(u(z_{i+1},t)-u(z_i,t))\frac{\Delta z_{i+1}}{\Delta z_i}+(u(z_i,t)-u(z_{i-1},t))\frac{\Delta z_i}{\Delta z_{i-1}}\right],i=2,3\cdots \tag{2}$$

where $t(z_i, t)$ is shear stress of soil at depth z_i; ρ is mass density of the soil; Δz_i is spacing interval between z_i and z_{i-1}; $a(z_i, t)$ is recorded acceleration at depth z_i; $u(z_i, t)$ is horizontal displacement at depth z_i and can be calculated through double integration of the corresponding recorded acceleration; $\gamma(z_i, t)$ is shear strain of soil at depth z_i.

Fig. 17 presented the stress-strain curves of soil in Case-1 and Case-2 at different depths under PGA=0.1 g and 0.15 g. Based on the previous

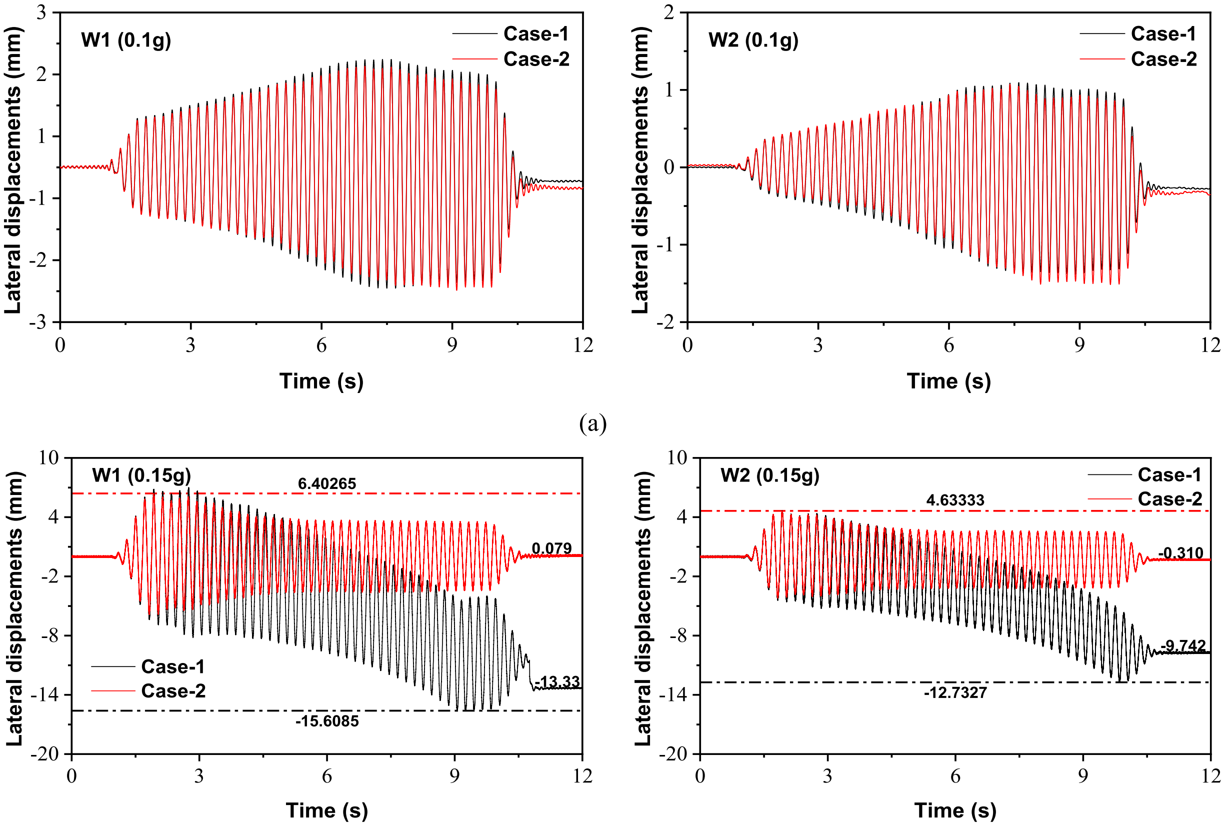

Fig. 13. Time histories of superstructure horizontal displacement for Case-1 and Case-2 at PGA of (a) 0.1 g and (b) 0.15 g.

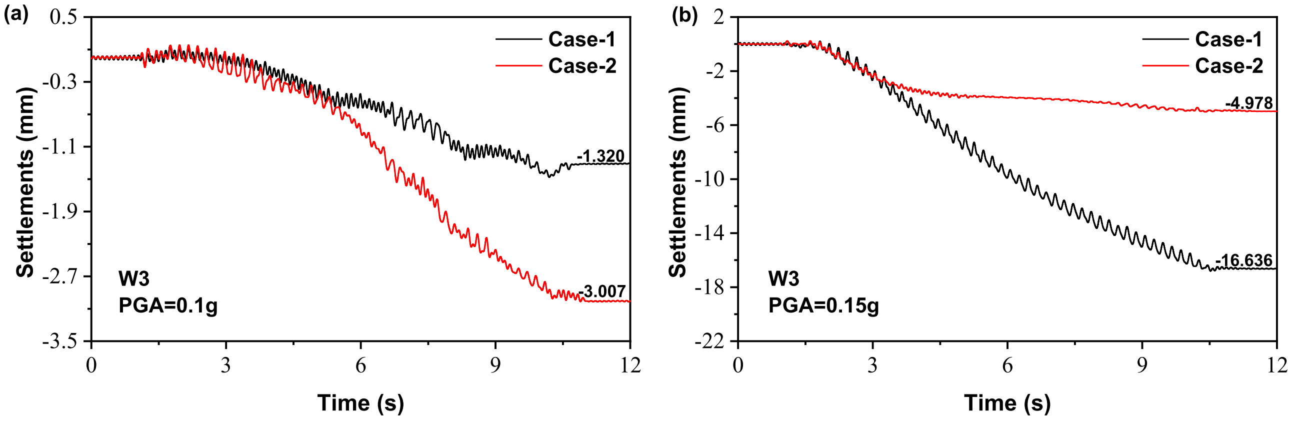

Fig. 14. Time histories of superstructure settlement for Case-1 and Case-2 at PGA of (a) 0.1 g and (b) 0.15 g.

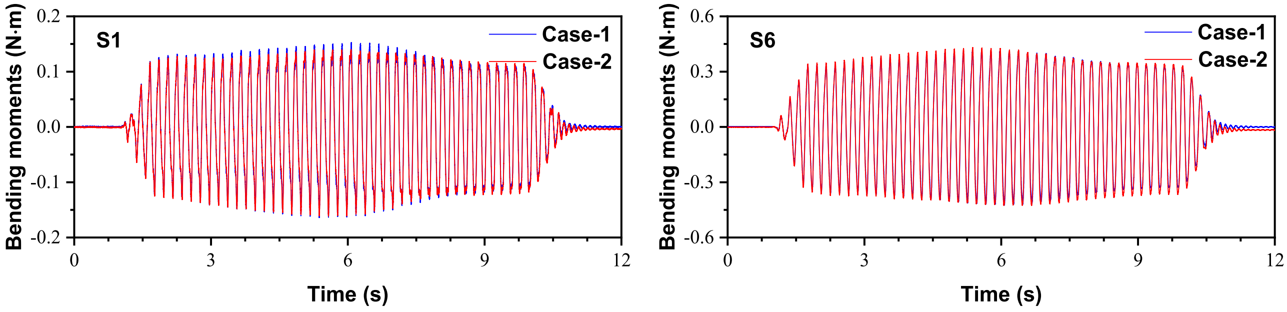

Fig. 15. Time histories of superstructure bending moment for Case-1 and Case-2 (PGA=0.1 g).

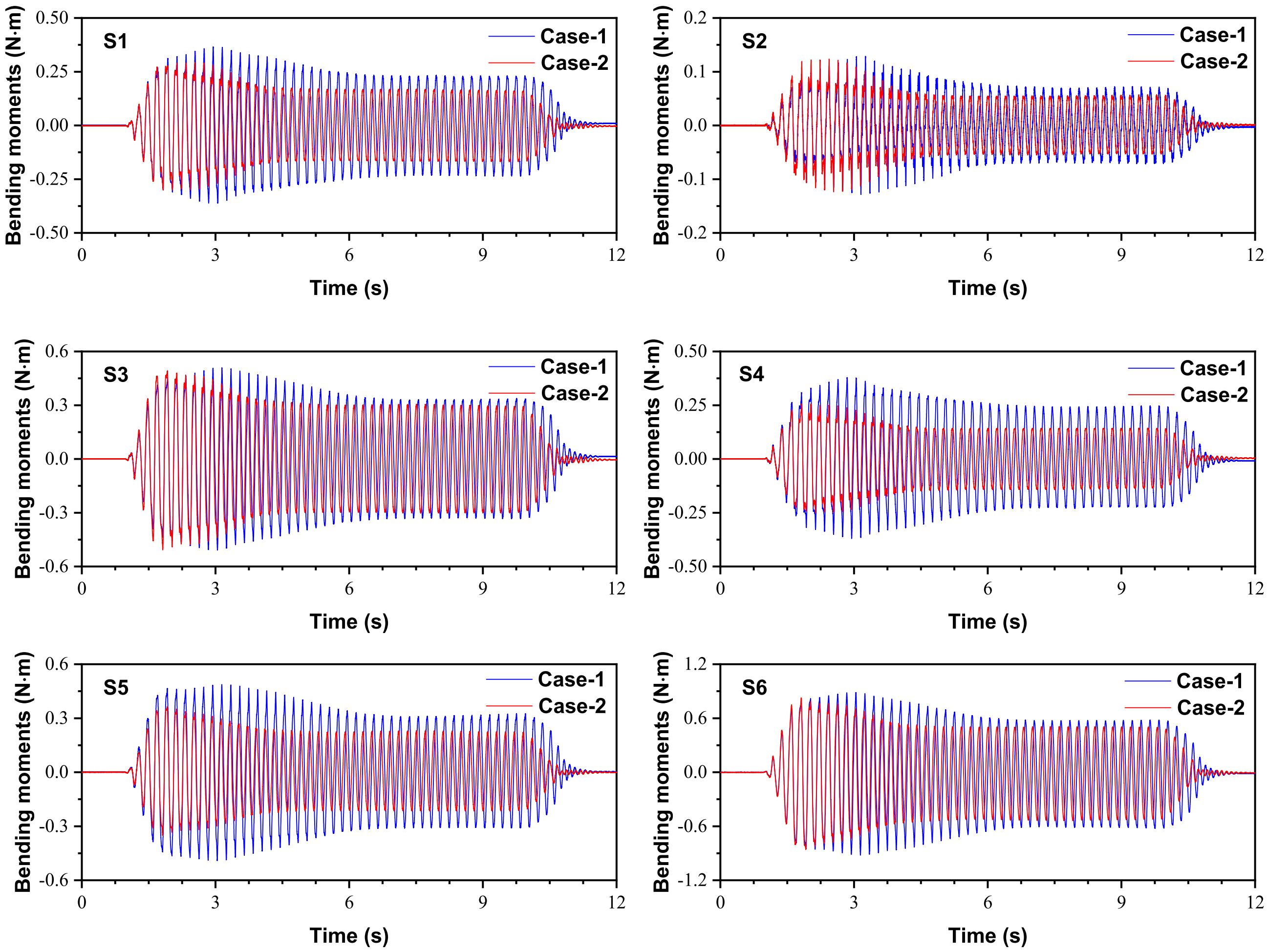

Fig. 16. Time histories of superstructure bending moment for Case-1 and Case-2 (PGA=0.15 g).

analysis, neither case reached the liquefaction state at PGA=0.1 g at any depth. As shown in Fig. 17(a), the hysteresis loops in Case-1 gradually steeper from 0.15 m to 0.35 m as vibration progresses, suggesting the excess water pressure decreased and an increase in soil stiffness. And the peak shear stresses were 0.41 kPa, 0.66 kPa, 0.91 kPa at depth of 0.15 m, 0.25 m and 0.35 m. The shear strength of the lower soil layer gradually increased. From the upper to the lower foundation layers, the shear strain decreased with depth. It highlighted the clear influence of overburden pressure and the coral silt layer in the bottom on the shear strength.

In Case-2, between 0.15 m and 0.25 m, the shear strain within the hysteresis loop increased, and the loop area expanded, indicating reduced shear strength at 0.25 m. However, from 0.25 m to 0.35 m, the loop edges steepened, and the strain decreased. At 0.35 m, the shear strength increased, likely due to the presence of coral silt in the middle layer. Comparing the stress-strain hysteresis curves of Case-1 and Case-2 at different depths under a 0.1 g load reveals that at a depth of 0.15 m, the constraint effect of the overburden load results in only a slight difference in soil stiffness. At a depth of 0.25 m, the presence of coral silt in Case-2 significantly reduces the shear strength and stiffness of this soil layer. By 0.35 m, the stiffness gradually recovers because of the overburden load.

Fig. 17(b) presented the hysteresis loops corresponding to Case-1 and Case-2 at diverse depths under a PGA of 0.15 g. A comprehensive comparison between Case-1 and Case-2 uncovered a conspicuous divergence in the evolution pattern of stress - strain curves across different depths when PGA=0.15 g. As seen in Fig. 17(b), the hysteresis loop of Case-1 at a depth of 0.15 m exhibits relatively large loop area and a flatten profile, accompanied by a comparatively substantial shear strain. At this juncture, the soil has already transitioned into the liquefaction state. As the depth increases along the curve, the loop becomes steeper, the shear strain decreases, the area of the hysteresis loop contracts, and the shear strength increases It can attribute to the overburden load. Regarding Case-2, the shear strain initially ascends and subsequently descends from the top towards deeper levels, and the area of the hysteresis loop followed an analogous pattern of variation. Zeghal et al. [40] in their investigation of the liquefaction response of a horizontal site via centrifuge shaking - table testing, discerned an identical pattern. Towards the conclusion of the shaking process, the sand layer manifested a relative upsurge in acceleration amplitude (signifying a concomitant enhancement in soil stiffness). It is posited that this restoration might be attributable, at least in part, to the densification and augmented interlocking of the sand skeleton. Gu et al. [17], during their exploration of the liquefaction - resistance attributes of sand intermingled with clayey fines using centrifuge shaking - table experimentation, procured comparable test outcomes; however, no subsequent phase of effective - stress recovery was observed. As depicted in Fig. 17 (b), within Case-1, the shear strain demonstrated a decreasing trend with increasing depth. Specifically, the terminal shear strain at depths of 0.15 m, 0.25 m and 0.35 m register at 0.48 %, 0.29 % and 0.16 %, respectively, indicating the effect of overburden pressure. As mentioned earlier, the coral silt layer affects the channeling of pore water transport through the foundation. It indicated that the coral silt layer also can decreased the stiffness of the foundation.

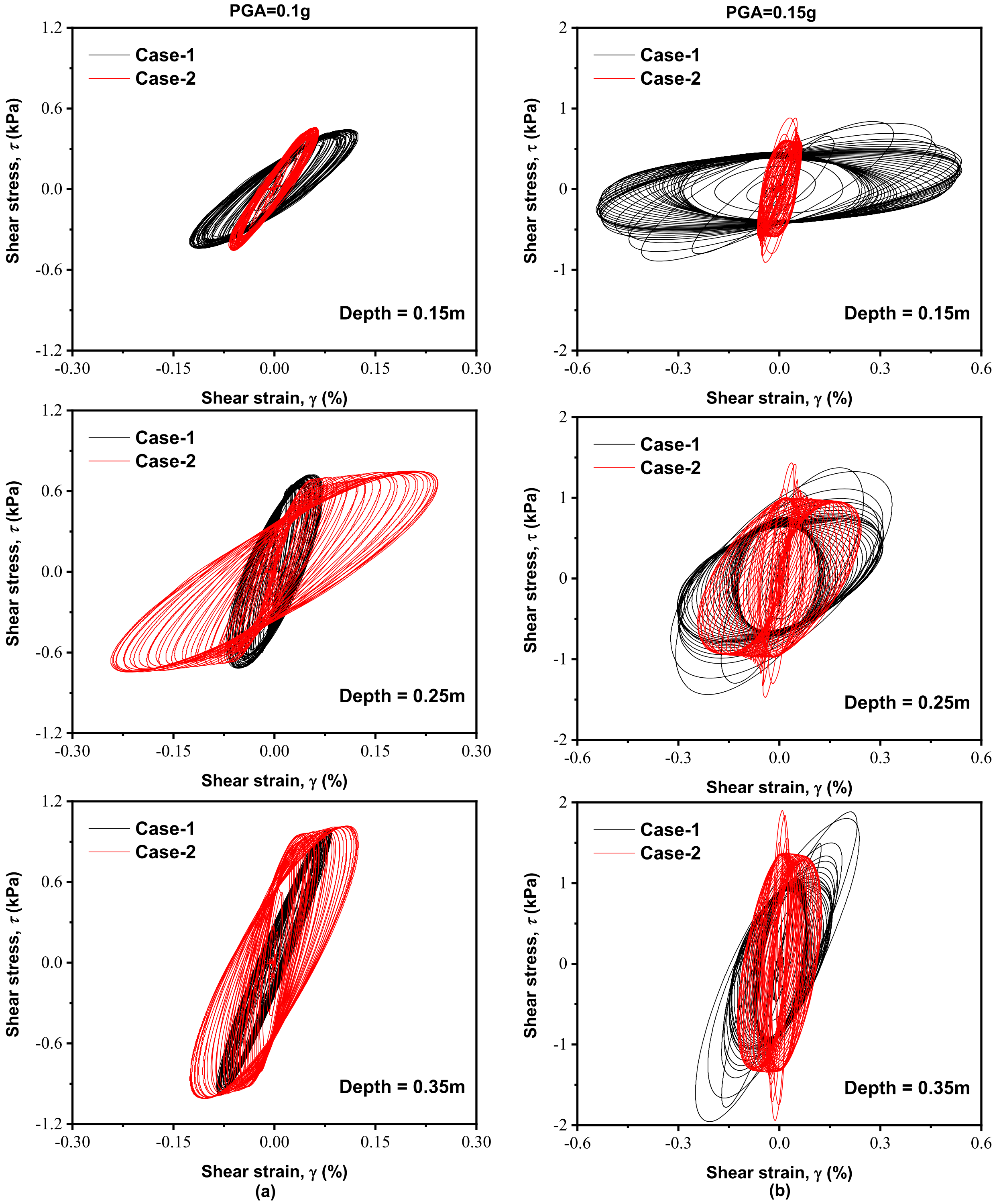

Fig. 17. Stress-strain curves of soil during shaking: (a) 0.1 g; and (b) 0.15 g.

4. Conclusions

In this research, two shaking table tests were conducted on a sand foundation with varying positions of a coral silt layer to investigate its impact on the dynamic response during seismic excitation. The key findings are as follows:

(1) The peak acceleration amplification factors progressively increased from the bottom to the top under varying amplitudes of seismic excitation. This indicates an amplification effect along the depth. Additionally, the overall stiffness of the foundation was greater when the coral silt was located in the middle compared to when it was at the bottom under seismic loading.

(2) Under seismic loading with a peak ground acceleration (PGA) of 0.1 g, the development of excess pore water pressure was

inhibited directly beneath the superstructure when the coral silt was in the middle of the foundation. The excess pore water pressure increased from the bottom to the top and was more pronounced in the coral silt region. When the coral silt layer was in the middle, it altered the distribution of the excess pore water pressure ratio, creating a turning point in the depth-distribution curve at the coral silt region. This significantly reduced excess pore water pressure in the upper region when the coral silt was situated in the middle.

(3) At a PGA of 0.1 g, the effective stress and stiffness of the foundation soil decreased only slightly, resulting in minimal lateral displacement and settlement of the superstructure, with only minor differences observed. However, at a PGA of 0.15 g, the presence of the coral silt layer significantly reduced both horizontal displacement and settlement.

(4) In both scenarios, shear strain decreased with depth, reflecting the influence of overburden pressure. At shallow depths, shear stiffness was greater when the coral silt was positioned in the middle of the foundation, especially at a PGA of 0.15 g. This increased stiffness is attributed to the coral silt layer's effect on pore water transport pathways within the foundation.

(5) The shaking table test was conducted under a 1 g condition. There is a certain difference in the stress level of the foundation compared to the actual condition. The test results can be used to qualitatively analyze the influence of coral mud interlayers on the dynamic response of the foundation under seismic load.

Funding

The work described in this paper was supported National Natural Science Foundation of China (Nos. U2268213 and 52108299), the Fundamental Research Funds for the Central Universities (Grant Nos. 2022CDJQY-012), The financial supports are gratefully acknowledged.

Data availability statement

Data generated or analyzed during this study are available from the corresponding author upon reasonable request.

CRediT authorship contribution statement

Chunyong Jiang: Writing – review & editing, Writing – original draft. **Xuanming Ding:** Writing – review & editing, Funding acquisition, Formal analysis. **Qiang Ou:** Writing – review & editing, Methodology, Funding acquisition, Conceptualization. **Jinqiao Zhao:** Writing – review & editing, Validation, Resources, Formal analysis, Data curation. **Zhaogang Luo:** Writing – review & editing, Validation, Software, Investigation, Conceptualization.

Declaration of competing interest

The authors declare that they have no known competing financial interests or personal relationships that could have appeared to influence the work reported in this paper.

References

[1] M. Adampira, M. Derakhshandi, A. Ghalandarzadeh, Experimental study on seismic response characteristics of liquefiable soil layers, J. Earthq. Eng. 25 (7) (2021) 1287–1315.
[2] T.G. Adonis, T.M. Michelle, S.Y Gong, H.M Hu, C.C Shen, F.P. Siringan, Coral boulder transport and gravel bar formation by storms in Lumaniag village, Batangas, northwestern Philippines, Geomorphology 376 (2021) 107554.
[3] ASTM, Standard Test Methods for Specific Gravity of Soil Solids by Water Pycnometer, D854 -14, ASTM International, West Conshohocken, PA, 2014.
[4] ASTM, Standard Test Methods for Maximum Index Density and Unit Weight of Soils Using a Vibratory Table, D4253 -16, ASTM International, West Conshohocken, PA, 2016.
[5] ASTM, Standard Test Methods for Minimum Index Density And Unit Weight Of Soils And Calculation Of Relative Density, D4254 -16, ASTM International, West Conshohocken, PA, 2016.
[6] MH. Baziar, MHM. Lashkajani, Prediction of excess pore water pressure generation in sand-silt mixtures during cyclic loading: a dissipated energy-based model, Geotechn. Geolog. Eng. 42 (6) (2024) 5209–5228.
[7] G.X. Chen, E.Q. Zhou, Z.H. Wang, B.H. Wang, X.J. Li, Experimental investigation on fluid characteristics of medium dense saturated fine sand in pre- and post-liquefaction, Bull. Earthq. Eng. 14 (8) (2016) 2185–2212.
[8] W. Cheng, Z.Y. Yin, Fractional order viscoplastic modeling of anisotropically overconsolidated clays with modified isotach viscosity, Int. J. Plasticity 172 (2024) 103858.
[9] W. Cheng, Z.Y. Yin, Y.J. Cui, M.Z. Peng, Non-isothermal fractional order two-surface viscoplastic model for stiff clays, Canad. Geotechn. J. (2024), https://doi.org/10.1139/cgj-2023-0701.
[10] M.A. Dehno, S R M Harami, MR. Noora, Environmental geochemistry of heavy metals in coral reefs and sediments of Chabahar Bay, Res. Eng. 13 (2022) 100346.
[11] X.M. Ding, Y.L. Zhang, Q. Wu, G.W. Cao, Z.X. Chen, Effects of groundwater level on the seismic responses of coral sand ground and superstructure by shaking table tests, Acta Geotechnica 17 (7) (2022) 3047–3066.
[12] X. Ding, Y. Zhang, Q. Wu, G. Cao, Z. Chen, Effects of groundwater level on the seismic responses of coral sand ground and superstructure by shaking table tests, Acta Geotechnica 17 (7) (2021) 3047–3066, https://doi.org/10.1007/s11440-021-01404-5.
[13] X.M. Ding, Y.L. Zhang, Q. Wu, Z.X. Chen, C.L. Wang, Shaking table tests on the seismic responses of underground structures in coral sand, Tunnelling Undergr. Space Technol. 109 (2021) 103775.
[14] A. Elgamal, Z.H. Yang, T. Lai, B.L. Kutter, D.W. Wilson, Dynamic response of saturated dense sand in laminated centrifuge container, J. Geotechn. Geoenviron. Eng. 131 (5) (2005) 598–609.
[15] X. Fang, C. Shen, H. Liu, C.Y. Wang, Y.X. Guo, P.X. Xiong, L.Q. Wang, Study on bearing characteristic of long-short-pile composite foundation with biocemented coral sand pile, Acta Geotech (2025), https://doi.org/10.1007/s11440-025-02552-8.
[16] Z.K. Feng, W.J. Xu, Q.S. Meng, Mechanical behaviors of interaction between coral sand and structure surface, J. Cent. South Univ. 27 (2020) 3436–3449.
[17] X.Q. Gu, D.S. Wu, K.L. Zuo, A. Tessari, Centrifuge Shake Table Tests on the Liquefaction Resistance of Sand with Clayey Fines, J. Geotech. Geoenviron. Eng. 148 (2) (2022) 04021180.
[18] P. Guo, G. Lei, L. Luo, X. Gong, Y. Wang, B. Li, X J Hu, H B Hu, Soil Creep Effect on Time-Dependent Deformation of Deep Braced Excavation, Adv. Mater. Sci. Eng. 2022 (1) (2022) 5655592.
[19] C.Y. Jiang, X.M. Ding, X.S. Chen, H.Q. Fang, Y. Zhang, Laboratory study on geotechnical characteristics of marine coral clay, J. Cent. South Univ. 29 (2) (2022) 572–581.
[20] X.L Jiang, H.D Wang, H. Yang, T. Du, P. Liu, J.X. Duan, Triaxial compression characteristics and brittleness evaluation of calcareous sand cemented with EICP and coir fiber, Res. Eng. 25 (2025) 104090.
[21] Y J Ju, M J Hu, Y. Liu, X. Zhu, KK. Qin, Formation process of underground freshwater based on zoning and stratification of coral reef island, Rock Soil Mech. 43 (5) (2022) 1226–1236.
[22] R. Kamai, R.W. Boulanger, Characterizing localization processes during liquefaction using inverse analyses of instrumentation arrays, Meso-Scale Shear Phys. Earthq. Landsl. mechan. (2010) 219–238.
[23] Kopf A, Fleischmann T, Gauchery T, et al. 2016. Report and preliminary results of R/V POSEIDON cruise POS500, LISA, Ligurian Slope AUV mapping, gravity coring and seismic reflection, Catania (Italy)–Malaga (Spain), 25.05. 2016–09.06. 2016.
[24] Y. Koga, O. Matsuo, Shaking table tests of embankments resting on liquefiable sandy ground, Soils Found. 30 (4) (1990) 162–174.
[25] S. Koutsourelakis, J.H. Prévost, G. Deodatis, Risk assessment of an interacting structure-soil system due to liquefaction, Earthq. Eng. Struct. Dyn. 31 (4) (2002) 851–879, https://doi.org/10.1002/eqe.125.
[26] W. Li, Y. Chen, A.W. Stuedlein, H. Liu, X. Zhang, Y. Yang, Performance of X-shaped and circular pile-improved ground subject to liquefaction-induced lateral spreading, Soil Dyna. Earthq. Eng. 109 (2018) 273–281.
[27] Z. Li, T. Chen, H. Liu, C. Ji, C. Zhu, C. Hu, Y.G. Jia, Earthquake response and post-earthquake stability assessment of submarine clay slopes, Appl. Ocean Res. 127 (2022) 103322.
[28] G.A. López Jiménez, D. Dias, O. Jenck, Effect of the soil–pile–structure interaction in seismic analysis: case of liquefiable soils, Acta Geotechnica 14 (5) (2018) 1509–1525, https://doi.org/10.1007/s11440-018-0746-2.
[29] M.J. Orang, R. Motamed, A. Prabhakaran, A. Elgamal, Large-Scale Shake Table Tests on a Shallow Foundation in Liquefiable Soils, J. Geotech. Geoenviron. Eng. 147 (1) (2021) 04020152.
[30] B. Rebecca, T.B Zoe, E.L Stephen, J.K Frederieke, N.W Scott, E.B Jon, D.M Silburn, Relating sediment impacts on coral reefs to watershed sources, processes and management: A review, Sci. Total Environ. 468-469 (2014) 1138–1153.
[31] S.J. Rui, Z. Guo, T.L. Si, Y.J. Li, Effect of particle shape on the liquefaction resistance of calcareous sands, Soil Dynam. Earthq. Eng. 137 (2020) 106302.
[32] N. Stark, R. Wilkens, V.B. Ernstsen, M. Lambers-Huesmann, S. Stegmann, A. Kopf, Geotechnical properties of sandy seafloors and the consequences for dynamic penetrometer interpretations: quartz sand versus carbonate sand, Geotech. Geolog. Eng. 30 (2012) 1–14, https://doi.org/10.1007/s10706-011-9444-7.
[33] T. Tomascik, A.J. Mah, A. Nontji, M.K. Moosa, The Ecol. Indones. Seas part 2, Tuttle Publishing, 2013.

[34] P. Wei, Z. Yin, C. Yao, Z. Ren, Y. Zheng, W. Ma, Atomistic origin of montmorillonite clay subjected to freeze-thaw hysteresis, J. Rock Mechan. Geotechn. Eng. (2025), https://doi.org/10.1016/j.jrmge.2024.11.004.

[35] D. Wu, K. Xu, P. Guo, G. Lei, K. Cheng, X. Gong, Ground deformation characteristics induced by mechanized shield twin tunnelling along curved alignments, Adv. Civil Eng. 2021 (1) (2021) 6640072.

[36] Q. Wu, X.M. Ding, Y.L. Zhang, Z.X. Chen, Comparative study on seismic response of pile group foundation in coral sand and fujian sand, J. Mar. Sci. Eng. (2020).

[37] D S Xu, H X Zhao, X C Fan, Y. Qin, Influence of spatial distribution of fine sand layers on the mechanical behavior of coral reef sand, Soil Dyna. Earthq. Eng. 169 (2023) 107897.

[38] T. Yao, Z.W. Cao, W. Li, On the mechanical behaviour of a coral silt from the South China Sea, Geotechnique, 2024, https://doi.org/10.1680/jgeot.24.00012.

[39] M. Zeghal, A.-W. Elgamal, H.T. Tang, J.C. Stepp, Lotung Downhole Array. II: Evaluation of Soil Nonlinear Properties, J. Geotechn. Eng. 121 (4) (1995) 363–378.

[40] M. Zeghal, A.-W. Elgamal, X. Zeng, K. Arulmoli, Mechanism of liquefaction response in sand–silt dynamic centrifuge tests, Soil Dynam. Earthq. Eng. 18 (1) (1999) 71–85.

[41] D.W. Zhang, A.H. Wang, X.M. Ding, Seismic response of pile groups improved with deep cement mixing columns in liquefiable sand: shaking table tests, Canad. Geotech. J. 59 (6) (2022) 994–1006.

[42] X.L. Zhang, Y.M. Chen, H.L. Liu, Z. Zhang, X.C. Ding, Performance evaluation of a MICP-treated calcareous sandy foundation using shake table tests, Soil Dyna. Earthq. Eng. 129 (2020) 105959.